PHOTONICS Research

Three-terminal germanium-on-silicon avalanche photodiode with extended p-charge layer for dark current reduction

Xiaobin Liu,[1] Xuetong Li,[1] Yuxuan Li,[1] Yingzhi Li,[1] Zihao Zhi,[1] Min Tao,[1] Baisong Chen,[1] Lanxuan Zhang,[1] Pengfei Guo,[2] Guoqiang Lo,[2] Xueyan Li,[1] Fengli Gao,[1] Bonan Kang,[1] and Junfeng Song[1,3,*]

[1]State Key Laboratory of Integrated Optoelectronics, College of Electronic Science and Engineering, Jilin University, Changchun 130012, China
[2]Advance Micro Foundry Pte Ltd, Singapore 117685, Singapore
[3]Peng Cheng Laboratory, Shenzhen 518000, China
*Corresponding author: songjf@jlu.edu.cn

Received 22 December 2021; revised 12 June 2022; accepted 13 June 2022; posted 13 June 2022 (Doc. ID 452004); published 28 July 2022

Germanium-on-silicon (Ge-on-Si) avalanche photodiodes (APDs) are widely used in near-infrared detection, laser ranging, free space communication, quantum communication, and other fields. However, the existence of lattice defects at the Ge/Si interface causes a high dark current in the Ge-on-Si APD, degrading the device sensitivity and also increasing energy consumption in integrated circuits. In this work, we propose a novel surface illuminated Ge-on-Si APD architecture with three terminals. Besides two electrodes on Si substrates, a third electrode is designed for Ge to regulate the control current and bandwidth, achieving multiple outputs of a single device and reducing the dark current of the device. When the voltage on Ge is −27.5 V, the proposed device achieves a dark current of 100 nA, responsivity of 9.97 A/W at −40 dBm input laser power at 1550 nm, and optimal bandwidth of 142 MHz. The low dark current and improved responsivity can meet the requirements of autonomous driving and other applications demanding weak light detection. © 2022 Chinese Laser Press

https://doi.org/10.1364/PRJ.452004

1. INTRODUCTION

Compared to the photodiode (PD), the avalanche photodiode (APD) can achieve higher sensitivity and quantum efficiency because of the internal gain mechanism. APD is widely used in optical sensing, quantum communication, LiDAR, and autonomous driving [1,2].

The III-V material-based APD suffers from high material cost and incompatibility with CMOS integration. These issues can be avoided by using germanium-on-silicon (Ge-on-Si) APDs. Being a small bandgap material, Ge has a strong linear absorption characteristic up to 1550 nm. The measured absorption coefficient is ~10,000 cm^{-1} at 1310 nm and ~5000 cm^{-1} at 1550 nm [3]. Its absorption range can be extended up to 1.6 μm by utilizing tensile strain-based bandgap engineering [4]. However, the large lattice mismatch (~4%) between Ge and Si results in a high dislocation density and makes it difficult to realize a high-quality epitaxial Ge layer on Si substrate. Despite great progress on the growth of Ge-on-Si in recent years [5], the problem of the large dark current caused by defects in Ge remains unsolved.

Meanwhile, the waveguide coupling method has been widely adopted to improve the responsivity of Ge-on-Si APDs [6–8]. Compared with the traditional surface illumination detector [9–11], the waveguide integrated APD has a much longer absorption length to achieve a higher response rate. However, this type of micro-nano optical structure is unable to collect the scattered light signal in the field of free space communication efficiently, rendering it unsuitable for the application of unmanned and LiDAR detection.

In this work, a three-terminal surface illuminated Ge-on-Si APD is proposed. Previously, Zheng *et al*. proposed a three-terminal Ge-on-Si APD [12–14]; its responsivity was 0.48 A/W, and it faces challenges to further optimize the dark current due to the stringent requirement of alignment accuracy between p-doped fingers and n-doped fingers. In our proposed structure, for the first time, we use an extended p-charge layer, separating the absorber region of germanium and the Si-APD region. Ge does not sit directly on top of the multiplication region, thus causing dark current reduction. In order to improve the output characteristics of the device, we introduce three electrodes to regulate and control the electric field. The electric field in the absorption region is controlled by the voltage on the Ge, and the multiplication is realized by the voltage on Si. By changing the applied voltages on Ge and Si, the

current and bandwidth of the APD can be optimized independently. The proposed device demonstrates a good responsivity of 9.97 A/W with a low dark current of 100 nA. The optimal bandwidth is 142 MHz, which is sufficient for application in free space optical communication. The low dark current and good responsivity enable the APD to be used in weak light detection and integrated in a large pixel array.

2. DEVICE OPERATION MECHANISM, DESIGN, AND FABRICATION

Traditional Ge-on-Si APDs generally require large electric fields to obtain large gains in the avalanche regions. The large electric field can easily deplete the charge layer and then extend into the Ge absorption layer. But there is a mass of dislocations in the epitaxial Ge absorption layer on Si due to the lattice mismatches at the interface. These dislocations can form thermal generation-recombination centers and, thus, induce a large dark current under a large electric field [15]. In order to solve this problem, we proposed a three-terminal Ge-on-Si APD structure, as shown in Fig. 1(a). It consists of two parts. One part provides a large gain, and it is a traditional two-electrode Si-APD structure [as shown on the right side of Fig. 1(a)]. This part of the structure has the excellent performance of Si-APD, low dark current and high gain, but this structure cannot respond to the near-infrared light. Therefore, the other part of the structure provides photoinduced charge, which is in the Ge absorption region. The Ge region can generate photogenerated carriers for near-infrared light, and this absorption region is controlled by an independent electrode. The novelty of the APD in this work is that the Ge absorption region and traditional two-electrode Si-APD structure are connected through an extended Si charge region as a bridge. This region separates the absorption region from the Si-APD region. The electric field in the Ge absorption region is mainly determined by the voltage on the Ge electrode, while the electric field in the multiplication region of Si is controlled by the voltage applied between n + + and p + + Si. The existence of this feature enables the device to respond to near-infrared light and achieve a high response at low dark current. At the same time, different outputs can be realized under different voltages applied to Ge. This is also useful for studying the influence of different electric fields in the Ge absorption region on photocurrent and bandwidth.

The devices were built on a silicon-on-insulator (SOI) wafer with 220 nm top-silicon, fabricated using the standard process in Advanced Micro Foundry (AMF), Singapore. Ge is grown by reduced pressure CVD (RPCVD), via selective Si epi growth. After the device is done, all the APDs are covered by oxide, which will help reduce the surface leakage current. The specific preparation steps of the device are as follows. The top-silicon layer was etched to define Si mesa patterns as shown in Fig. 1(b). Boron and phosphorus were implanted on the wafers to form p-type and n-type regions, respectively. The p + + and n + + regions are the two terminals for Si. The Ge layer was then epitaxially grown on a light p-type region [highlighted in pink in Fig. 1(b)]. The dimension of the epitaxial Ge is 30 μm (diameter) × 30 μm (diameter) × 720 nm (height). The Ge film was intrinsic by growth and was subsequently

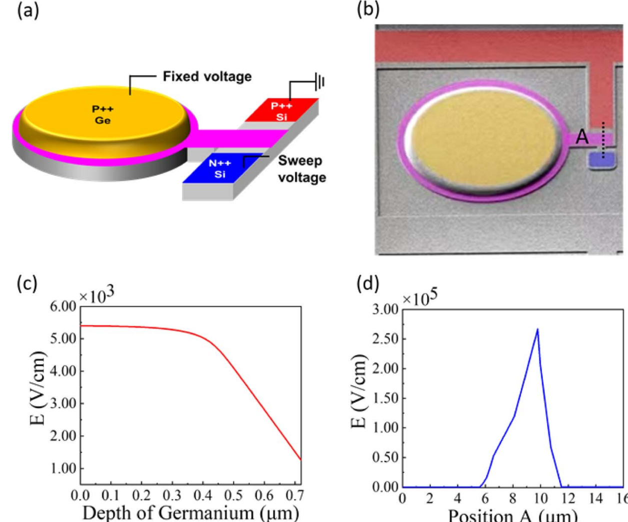

Fig. 1. (a) Structural diagram of three-terminal Ge-on-Si APD. (b) SEM image of pixel units. (c) Electric field simulation diagram of Ge region. (d) Simulated electric field in Si APD area [electric field at different positions of line A in (b)].

implanted to form p + + Ge at the top surface and thus to form the Ge terminal contact.

Simulation was performed to examine the electric field in the device using TCAD software. Because the structure is three-dimensional and cannot be simplified in both the horizontal and vertical directions, three-dimensional device simulation is used. Figure 1(c) shows the simulated electric field in the germanium region. Figure 1(d) shows the electric field between the two electrodes of p + + and n + + Si. The electric fields in Figs. 1(c) and 1(d) were obtained with 55 V being applied on the n + + Si terminal, while p + + Si is at ground potential and Ge terminals are floated. It is observed that, at a breakdown voltage of 55 V, the electric field in the Si avalanche region is 2.7×10^5 V/cm, larger than the threshold electric field triggering avalanche multiplication in Si. At the same time, the low electric field in the Ge layer is beneficial for dark current reduction by suppressing undesired avalanche breakdown in Ge [16]. However, the low electric field in Ge will cause a low responsivity. Therefore, the voltage on the Ge terminal needs to be adjusted to improve the device responsivity while maintaining a low dark current.

3. DEVICE CHARACTERIZATION

A. Two-Terminal *I-V* Characteristics and Responsivity

The APD was characterized using the Keysight N7714A laser as the light source. Light was illuminated directly above the Ge active layer of the detectors through single mode fiber. Meanwhile, the probes contacted the APD's electrode pads, which are connected to the Keysight 4200-SCS for data reading.

Due to the complexity of three-terminal APD, the device can be used as a traditional APD by floating one of the electrodes. The first configuration is to float the electrode on Ge

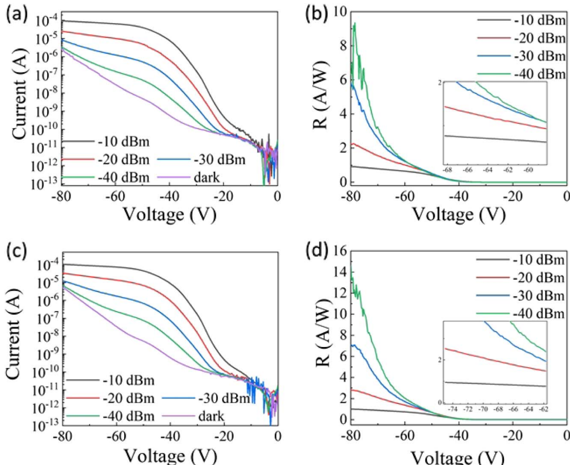

Fig. 2. (a) Current characteristic diagram at 1550 nm under different input optical power. (b) Responsivity characteristic diagram at 1550 nm under different input optical power. (c) Current characteristic diagram at 1310 nm under different input optical power. (d) Responsivity characteristic diagram at 1310 nm under different input optical power. The figure shows the voltage applied to two terminals Ge and n + + Si.

and make the APD region in Si reversely biased. The observed light response is very weak because photo carriers in Ge cannot be swept into the APD region in Si to form a photocurrent. The second configuration is to apply reverse bias between Ge and the n + + Si terminal. The photocurrent of the APD was measured as a function of incident light power at both 1310 and 1550 nm. As shown in Figs. 2(a) and 2(c), when the dark current is greater than 0.1 nA, the device will generate a significant photocurrent under low input optical power. Due to the increase of the electric field inside Ge, the photogenerated carriers in Ge sweep into the avalanche region in Si to form a photocurrent. The responsivity of the device under different input light powers is shown in Figs. 2(b) and 2(d). When dark current is 100 nA, the device has a responsivity of 1.29 A/W and 1.63 A/W at 1550 nm and 1310 nm, respectively, when the input laser power is −20 dBm.

B. Three-Terminal *I-V* Characteristics and Responsivity

To better understand the device physics of three-terminal APD, three-dimensional simulation with TCAD software was performed. A fixed voltage is applied on the Ge electrode, and the p + + Si terminal is at ground, while the voltage varies on n + + Si terminal. According to our initial simulation results, this voltage application mode can adjust the dark current. At the same time, the three electrode voltage application mode also best reflects the distinction between the three-terminal-based APD and the conventional APD. In previous reports of APDs, the output characteristics of this voltage application method were not specifically reported, even if it was a three-terminal device, such as in Ref. [12].

The trend of the simulated current is consistent with the measured results as shown in Figs. 3 and 4(a), and the electric field from TCAD software simulation is depicted in Fig. 5. Figure 5(b) shows the electric field in Si along the n + + to

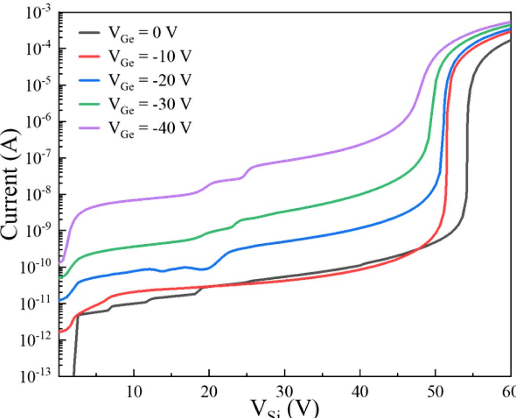

Fig. 3. It represents the simulated dark current diagram (current output at the n + + terminal) when different fixed voltages are applied to Ge when the n + + Si voltage is 60 V and p + + Si is grounded.

p + + direction when different voltage biases were applied on the Ge terminal, ranging from 0 to −40 V. It shows that the voltage on Ge has negligible impact on the electric field inside Si. This phenomenon is attributed to the existence of the bridge region, which separates the Ge from the Si region. In Fig. 5(d), the simulated electric field in Ge increases with the increase of applied voltage in the Ge region. It is obvious from Figs. 3 and 4(a) that dark current increases with the increase of applied voltage. When the voltage on Ge is −40 V, the electric field in Ge is about 1.3×10^4 V/cm [see Fig. 5(d)], and the initial dark current is still at nA level.

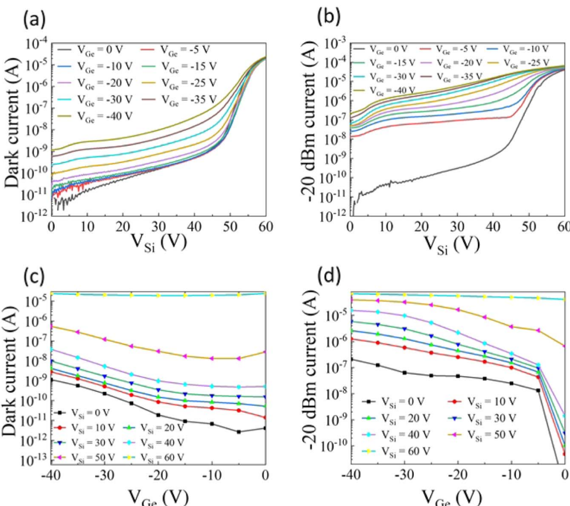

Fig. 4. When the n + + Si terminal scanning voltage is 60 V, the p + + Si terminal is grounding, and different fixed voltages are applied to Ge: (a) dark current; (b) current characteristic diagram at 1550 nm under input optical power −20 dBm. (c) Under the fixed Si voltage, the dark current of n + + Si terminal varies with the applied voltage of Ge. (d) Under the fixed Si voltage, the current at 1550 nm at an input optical power of −20 dBm varies with the applied voltage of Ge.

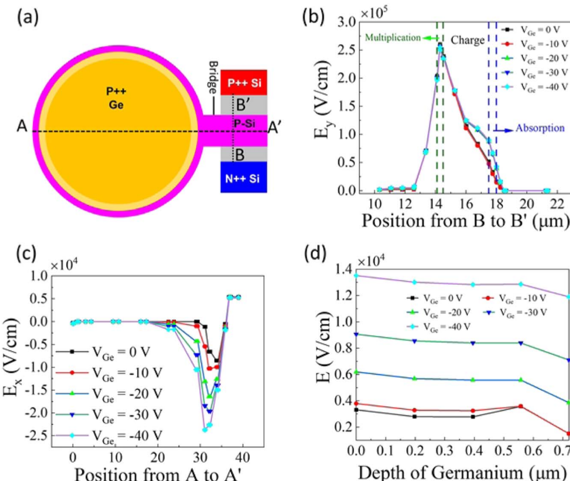

Fig. 5. (a) Schematic diagram of three-terminal APD. (b) Y direction electric field simulation in Si region [position from B to B' in (a)]. (c) X direction electric field simulation of Si charge region [position from A to A' in (a)]. (d) Electric field simulation diagram of Ge region.

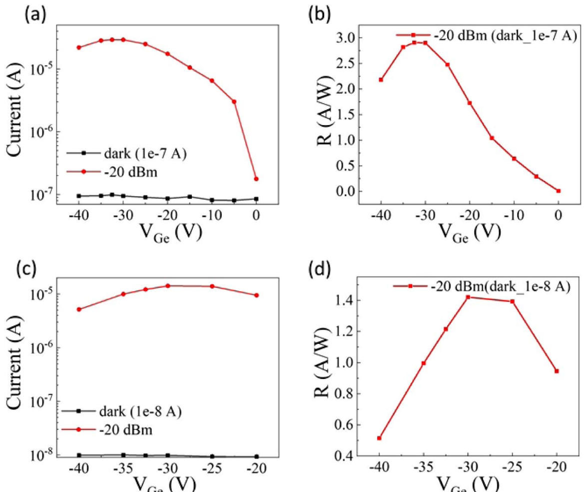

Fig. 6. (a) Photocurrent diagram at 10^{-7} A. (b) Responsivity at 10^{-7} A. (c) Photocurrent diagram at 10^{-8} A. (d) Responsivity at 10^{-8} A.

Due to the existence of the bridge region [see Fig. 5(a)], the Ge absorption region and the Si multiplication region are separated. As shown in Fig. 5(c), we can see that E_x increases with the increase of the voltage applied to Ge, which makes more carriers enter the Si multiplication region through the bridge region and realize the avalanche and multiplication effects. In summary, this structure can control the electric field in Ge by changing the voltage in Ge, while the avalanche amplification electric field in the Si region is basically unaffected.

Dark current at different voltages on Ge was measured, as shown in Fig. 4(a). As expected, the dark current increases with the increase of the applied voltage on the Ge electrode. The difference in breakdown voltage (defined as the voltage when dark current is 10^{-5} A) is less than 2 V as the voltage on Ge changes from 0 to −40 V. From Figs. 4(c) and 4(d), when the voltage of the n + + terminal is kept constant, the dark current and photocurrent increase with the increase of the voltage applied to Ge. The increase of the photocurrent is greater than the dark current. This method of applying voltage can improve the responsivity of the device, but it is also accompanied by an increase in dark current. From Figs. 4(a) and 4(b), we can extrapolate the responsivity under different applied Ge voltages in order to obtain the best operating voltage range on Ge. Responsivity of the device was measured with input light power of −20 dBm at 1550 nm for different voltages on Ge. Responsivity of APD is commonly defined near the breakdown voltage. Under such bias condition, the dark current is usually high, leading to a high noise level, despite good responsivity [17–19]. In this work, a new method to extract the responsivity is adopted. The extracted responsivity can serve as a figure-of-merit for practical applications in low light detection. We used two low dark current levels at 10^{-7} A and 10^{-8} A. From Fig. 6, we can find that the high responsivity can be achieved by changing the voltage on Ge. We can clearly see that the device has the best working voltage (voltage on Ge). By comparison, we selected the voltage of −27.5 V on the Ge as the optimal point and tested its multiple input optical power as shown in Figs. 7(a) and 7(c).

We define the responsivity of the 10^{-7} A dark electric flow level, which is labeled R_1. We define the responsivity of the 10^{-8} A dark electric flow level, which is labeled R_2. As shown in Figs. 7(b) and 7(d), we calculated R_1 and R_2 at this voltage. As shown in Table 1, even when the dark current is 10^{-8} A and R_2 is at 1550 nm, the laser responsivity is 2.07 A/W at −40 dBm, and you can clearly see the good responsivity of the device in weak light condition. From Table 1, we can find that the responsivity has different magnitudes under different input optical powers. When the incident optical power is −10 dBm, the germanium absorption layer will

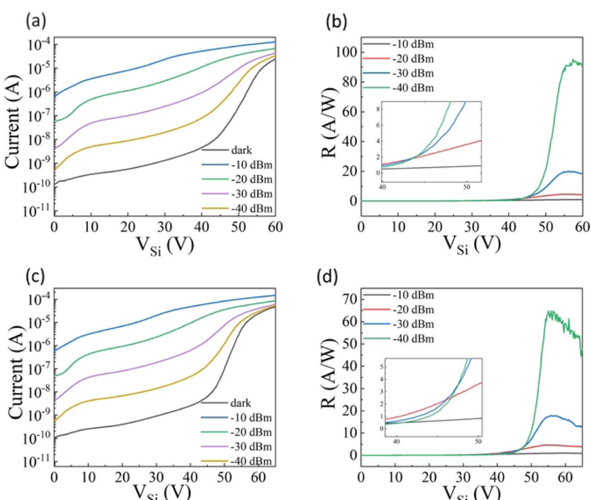

Fig. 7. When the voltage on Ge is −27.5 V. (a) Current characteristic diagram at 1310 nm under different input optical power. (b) Responsivity characteristic diagram at 1310 nm under different input optical power. (c) Current characteristic diagram at 1550 nm under different input optical power. (d) Responsivity characteristic diagram at 1550 nm under different input optical power.

Table 1. Response of Ge to −27.5 V at Different Input Power

	−10 dBm	−20 dBm	−30 dBm	−40 dBm
R_1 at 1310 nm	0.80 A/W	3.16 A/W	6.17 A/W	10.50 A/W
R_2 at 1310 nm	0.63 A/W	1.80 A/W	1.82 A/W	1.74 A/W
R_1 at 1550 nm	0.83 A/W	3.55 A/W	6.96 A/W	9.97 A/W
R_2 at 1550 nm	0.68 A/W	2.36 A/W	2.48 A/W	2.07 A/W

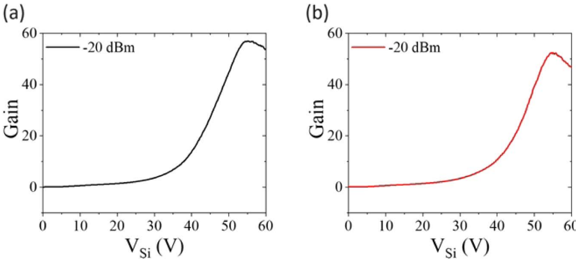

Fig. 8. When the voltage on Ge is −27.5 V. (a) Avalanche gain at 1310 nm wavelength. (b) Avalanche gain at 1550 nm wavelength.

generate a large number of photogenerated carriers, resulting in the space charge effect [20] and reducing the responsivity. When the incident optical power is weak (−20 dBm and below), the responsivity has a relatively fixed value (see Table 1, R_2) at low voltage. But with the increase of the applied voltage, the avalanche gain is too large and close to saturation, which makes the responsivity change greatly. Typically, the gain of an APD also decreases with increasing optical power [17,21,22]. This also causes the responsivity at high voltage to decrease with increasing input power (see Table 1, R_1).

When the voltage on Ge is −27.5 V, the punch-through voltage of the APD is around 15 V, and the breakdown voltage is around 56 V. Figures 8(a) and 8(b) show the gain curves of the APD at 1310 nm and 1550 nm, respectively, when the input optical power is −20 dBm. The responsivity of APD is lower at unity gain, both around 0.08 A/W (at 1310 nm and 1550 nm). When the dark current of APD reaches 10 nA, the gain of the photocurrent at both 1310 nm and 1550 nm is greater than 20. The large gain improves the responsivity and sensitivity of the APD but also limits the bandwidth to a certain extent. As shown in Fig. 9, we provide the responsivity of the device in different bands, which proves that the device has good spectral characteristics. It reflects the ability of Ge material to

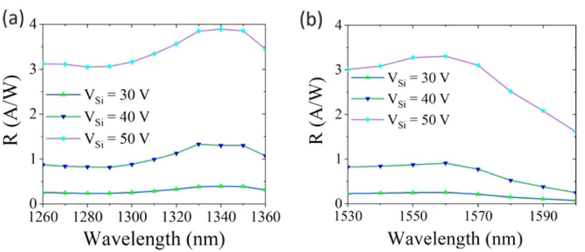

Fig. 9. When the applied voltage on p + + Ge is −27.5 V and the input optical power is −20 dBm. (a) Responsivity in O-band. (b) Responsivity in C-band (1530–1560 nm) and L-band (1570–1600 nm).

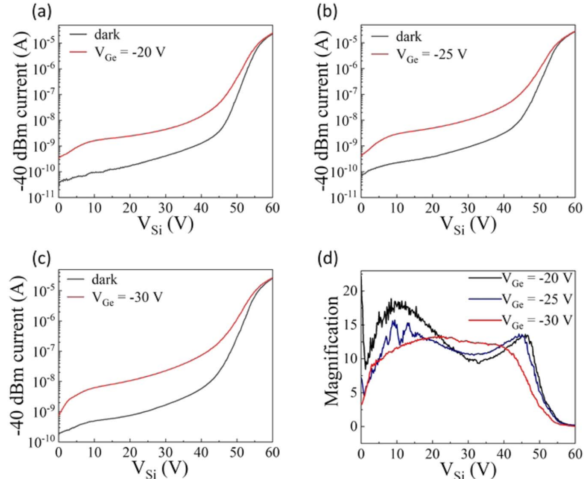

Fig. 10. (a) Current at −20 V on Ge. (b) Current at −25 V on Ge. (c) Current at −30 V on Ge. (d) At different voltages on Ge, the photocurrent is greater than the multiple of dark current.

absorb light of different wavelengths, which proves that the device has good optoelectronic properties in the communication band.

In order to verify the good detection characteristics of the device under weak light condition, we have compared the light and dark current of 1550 nm laser when the input power is −40 dBm and the voltage is −20 to −30 V on Ge. From Figs. 10(a)–10(c), we can calculate the magnification of photocurrent relative to dark current. In Fig. 10(d), we can find that the magnification is mostly over 10, and the difference between the photocurrent and dark current can be well distinguished. It shows that the device has good detectability for weak light.

4. DEVICE EQUIVALENT CIRCUIT MODEL

The electric circuit model of a three-terminal Ge-on-Si APD is much more complex than that of a conventional two-terminal APD [23] because multiple current paths exist between any two of the three electric terminals. In order to analyze the bandwidth property of this APD, radio frequency (RF) response characteristics from 10 to 600 MHz of it are measured using the Keysight N4373D Lightwave Component Analyzer. To simplify the measurement, we used a GS probe to load on the electrodes of p + + Si and n + + Si, and we used a source pressure meter to add voltage to the Ge electrode. The normalized RF response characteristics of APD at different voltages of Si when Ge voltage is −27.5 V are shown in Fig. 11(a). When the Si voltage is 20 V, the maximum bandwidth of 3 dB is 142 MHz. At this point, the device has been fully punched through, and the carriers have reached the saturation velocity. With the increase of the applied voltage, the multiplication enhancement bandwidth decreases. As shown in Fig. 11(b), when the Ge bias voltage is fixed, the reflected impedance curve of this APD expands with the Si port bias voltage increasing, which is due to the enhancement of the space charge effect [21,22]. From Figs. 11(c) and 11(d), we can see that, when the voltage on Si is constant, the figure is 15 V, and changing the voltage on Ge has little effect on the parameters of S22,

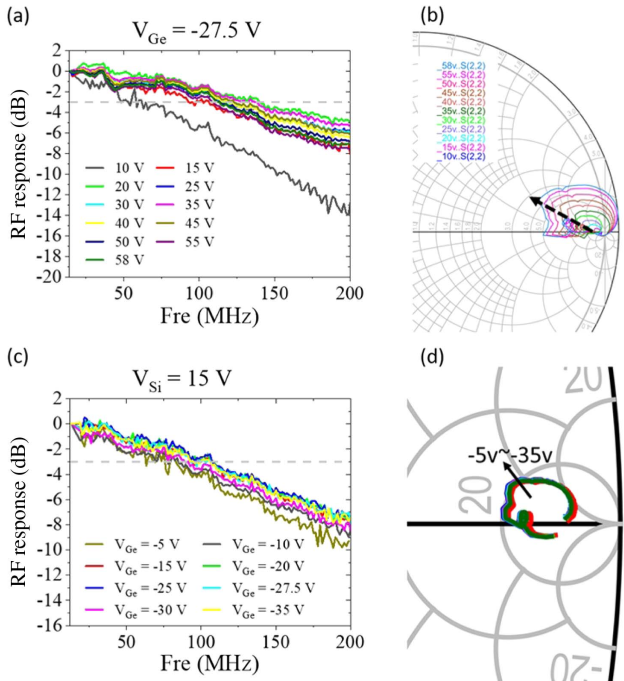

Fig. 11. (a) The APD has a normalized RF response characteristic at a voltage of Ge at −27.5 V and different Si input voltages. (b) The APD voltage on the Ge is −27.5 V, and the S22 parameters are measured under different Si input voltages. (c) The APD has a normalized RF response characteristic at a voltage of Si at 15 V and different Ge input voltages. (d) The APD voltage on the Si is 15 V, and the S22 parameters are measured under different Ge input voltages [the specific voltage values are shown in (c)].

so changing the voltage on Ge has little effect on the bandwidth. When the voltage on Ge is −5 V, the minimum 3 dB bandwidth is 70 MHz. For the existing LiDAR ranging system [24–26] with an integrated optical phased array chip,

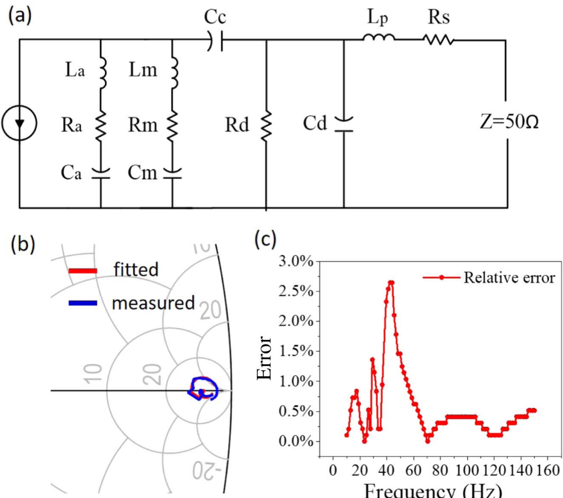

Fig. 12. (a) When the voltage is −27.5 V on Ge, the three-terminal APD equivalent circuit model. (b) When the signal ends are input to 15 V, the reflection coefficient is measured and fitted. (c) The relative error values between simulation and practice in (b).

Table 2. Fitted Electric Circuit Parameters of a Three-Terminal Avalanche Photodiode under a Reverse Bias of 15 V

Parameters	L_p (nH)	R_s (kΩ)	C_d (fF)	R_d (kΩ)
Values	1375	1.21	45	2.41
Parameters	C_c (pF)	L_m (μH)	R_m (kΩ)	C_m (pF)
Values	2.8	19.8	0.825	4.2
Parameters	L_a (μH)	R_a (kΩ)	C_a (fF)	
Values	196	1	172	

the 3 dB bandwidth of MHz can meet its measurement requirements.

In order to understand the measured S22 parameters of the three-terminal APD in Fig. 11(b), the electric circuit diagram of the APD is shown in Fig. 12(a). Circuit elements (capacitances, inductances, and resistances) are grouped together [27–29]. Specifically, the three-terminal APD's electrical impedance includes those of the diode junction and the electrodes. Here, L_p is the parasitic inductance of the electrodes. R_s is the ohmic contact resistance from metal electrodes and the semiconductor. C_d is the capacitance of depletion region, which includes the absorption region, charge region, and multiplication region. R_d is the resistance of the depletion region, which includes the absorption region, charge region, and multiplication region. C_c is the capacitance of the charge region. L_m, C_m, and R_m originate from the multiplication region of Si. Because the space charge effect appears in the multiplication region at a large gain [30–32], the carriers generated by multiplication will change rapidly, causing a change of the local current, charge, and carrier velocity. L_a, C_a, and R_a originate from the absorption region of Ge on the left side of the bridge and are generated by the accumulation of photogenerated carriers in it. The values of these parameters are fitted by S22 parameters, and an example of 15 V is shown in Fig. 12(b). The relative error between the fitted S parameter and the measured is less than 3%, which can be found in Fig. 12(c). The detailed values of the fitting parameters are shown in Table 2.

5. CONCLUSION

We propose a new Ge-on-Si APD structure, which uses the extended p-charge layer to separate the Ge absorption and Si-APD region. We use Si material with low-noise properties as the multiplication region to reduce the excess noise of the APD [33]. By introducing three electrodes to control the electric fields in the absorption and avalanche region, respectively, the goals of low dark current and high responsivity of the surface-illuminated detector are achieved. Before us, the responsivity of surface illumination devices was very low, and high responsivity could only be achieved with a large dark current. We widened the limit of weak light detection to −40 dBm. Under the input light power of −40 dBm, R_1 at 1310 nm is 10.5 A/W and R_1 at 1550 nm is 9.97 A/W. The device performance is much better than that of other surface illumination devices, which is shown in Table 3. These characteristics make the device able to be used in laser radar,

Table 3. Device Performance of Surface Illuminated APDs

Reference	λ (nm)	Dark Current (A)	Responsivity (A/W)
[34]	1310	8.4×10^{-7}	6.54
[10]	1310	10^{-5}	12.00
[35]	1550	10^{-4}	12.70
[36]	1310	10^{-6}	4.40
[33]	1310	$\sim10^{-6}$	5.88
This work	1310	10^{-7}	10.50
This work	1550	10^{-7}	9.97

weak light imaging, and other fields. In the LiDAR system, a boost circuit can be used to power our APD. It has high responsivity when the input optical power is only −40 dBm, which opens a new avenue to further improve the performance of LiDAR receivers [22]. Of course, the speed of the device is relatively slow, mainly due to the relatively long transit time of the photogenerated carriers from the absorption region of Ge through the bridge to the avalanche region, and 3 dB bandwidth is only 142 MHz. In the future, it is possible to consider reducing the size of the device or adjusting the doping concentration on the connecting bridge to increase the electric field and further reduce the transit time of electrons.

This new type of APD can be manufactured with a high yield in a standard CMOS process. The different performance indicators of this APD, such as breakdown voltage, can be realized on the same wafer by design. The three-terminal APD has broken the inherent barrier of the single output of the previous APD device. This is the first and a major breakthrough.

Funding. Program for Jilin University Science and Technology Innovative Research Team (JLUSTIRT, 2021TD-39); Jilin Scientific and Technological Development Program (20200501007GX); National Natural Science Foundation of China (61627820, 61934003, 62090054).

Disclosures. The authors declare that there are no conflicts of interest related to this article.

Data Availability. Data underlying the results presented in this paper are not publicly available at this time but may be obtained from the authors upon reasonable request.

REFERENCES

1. J. Zhang, M. A. Itzler, H. Zbinden, and J. W. Pan, "Advances in InGaAs/InP single-photon detector systems for quantum communication," Light Sci. Appl. **4**, e286 (2015).
2. M. Wanitzek, M. Oehme, D. Schwarz, K. Guguieva, and J. Schulze, "Ge-on-Si avalanche photodiodes for LIDAR applications," in *43rd International Convention on Information, Communication and Electronic Technology (MIPRO)* (2020), pp. 8–12.
3. V. Sorianello, A. Perna, L. Colace, G. Assanto, H. C. Luan, and L. C. Kimerling, "Near-infrared absorption of germanium thin films on silicon," Appl. Phys. Lett. **93**, 111115 (2008).
4. Y. Ishikawa, K. Wada, D. D. Cannon, J. Liu, H.-C. Luan, and L. C. Kimerling, "Strain-induced band gap shrinkage in Ge grown on Si substrate," Appl. Phys. Lett. **82**, 2044–2046 (2003).
5. J. M. Hartmann, A. Abbadie, A. M. Papon, P. Holliger, G. Rolland, T. Billon, J. M. Fédéli, M. Rouvière, L. Vivien, and S. Laval, "Reduced pressure-chemical vapor deposition of Ge thick layers on Si(001) for 1.3–1.55-μm photodetection," J. Appl. Phys. **95**, 5905–5913 (2004).
6. H. T. Chen, J. Verbist, P. Verheyen, P. De Heyn, G. Lepage, J. De Coster, P. Absil, B. Moeneclaey, X. Yin, J. Bauwelinck, J. Van Campenhout, and G. Roelkens, "25-Gb/s 1310-nm optical receiver based on a sub-5-V waveguide-coupled germanium avalanche photodiode," IEEE Photon. J. **7**, 7902909 (2015).
7. A. Palmieri, M. Vallone, M. Calciati, A. Tibaldi, F. Bertazzi, G. Ghione, and M. Goano, "Heterostructure modeling considerations for Ge-on-Si waveguide photodetectors," Opt. Quantum Electron. **50**, 71 (2018).
8. Z. Huang, C. Li, D. Liang, K. Yu, C. Santori, M. Fiorentino, W. Sorin, S. Palermo, and R. G. Beausoleil, "25 Gbps low-voltage waveguide Si–Ge avalanche photodiode," Optica **3**, 793–798 (2016).
9. W. S. Zaoui, H.-W. Chen, J. E. Bowers, Y. Kang, M. Morse, M. J. Paniccia, A. Pauchard, and J. C. Campbell, "Frequency response and bandwidth enhancement in Ge/Si avalanche photodiodes with over 840 GHz gain-bandwidth-product," Opt. Express **17**, 12641–12649 (2009).
10. Y. Kang, M. Zadka, S. Litski, G. Sarid, M. Morse, M. J. Paniccia, Y. H. Kuo, J. Bowers, A. Beling, H. D. Liu, D. C. McIntosh, J. Campbell, and A. Pauchard, "Epitaxially-grown Ge/Si avalanche photodiodes for 1.3 μm light detection," Opt. Express **16**, 9365–9371 (2008).
11. G. Kim, S. Kim, S. A. Kim, J. H. Oh, and K.-S. Jang, "NDR-effect vertical-illumination-type Ge-on-Si avalanche photodetector," Opt. Lett. **43**, 5583–5586 (2018).
12. X. Zeng, Z. Huang, B. Wang, D. Liang, M. Fiorentino, and R. G. Beausoleil, "Silicon-germanium avalanche photodiodes with direct control of electric field in charge multiplication region," Optica **6**, 772–777 (2019).
13. B. Wang, Z. Huang, X. Zeng, D. Liang, M. Fiorentino, and R. G. Beausoleil, "35 Gb/s ultralow-voltage three-terminal Si-Ge avalanche photodiode," in *Optical Fiber Communications Conference and Exhibition (OFC)* (2019), paper Th3B.2.
14. X. Zeng, Z. Huang, D. Liang, M. Fiorentino, and R. G. Beausoleil, "Low-voltage three-terminal avalanche photodiodes," in *Conference on Lasers and Electro-Optics* (2017), paper SF2I.3.
15. D. Benedikovic, L. Virot, G. Aubin, J.-M. Hartmann, F. Amar, X. Le Roux, C. Alonso-Ramos, É. Cassan, D. Marris-Morini, J.-M. Fédéli, F. Boeuf, B. Szelag, and L. Vivien, "Silicon-germanium receivers for short-wave-infrared optoelectronics and communications high-speed silicon-germanium receivers," Nanophotonics **10**, 1059–1079 (2021).
16. Z. Huang, X. Zeng, D. Liang, M. Fiorentino, and R. G. Beausoleil, "Operation and analysis of low-voltage three-terminal avalanche photodiodes," in *IEEE 14th International Conference on Group IV Photonics (GFP)* (2017), pp. 174–175.
17. L. Virot, P. Crozat, J.-M. Fédéli, J.-M. Hartmann, D. Marris-Morini, E. Cassan, F. Boeuf, and L. Vivien, "Germanium avalanche receiver for low power interconnects," Nat. Commun. **5**, 4957 (2014).
18. Y. Li, X. Luo, G. Liang, and G.-Q. Lo, "Demonstration of Ge/Si avalanche photodetector arrays for lidar application," in *Optical Fiber Communication Conference* (2019), paper TU3E.3.
19. M. Huang, S. Li, P. Cai, G. Hou, T.-I. Su, W. Chen, C.-Y. Hong, and D. Pan, "Germanium on silicon avalanche photodiode," IEEE J. Sel. Top. Quantum Electron. **24**, 3800911 (2018).
20. K. He, J. Lu, X. Ma, Y. Ju, L. Xie, L. Pang, X. Wang, and J. Chen, "Effect of Maxwell–Wagner relaxation on field charging of particles," Aerosol Sci. Technol. **49**, 1210–1221 (2015).
21. D. Dai, M. Piels, and J. E. Bowers, "Monolithic germanium/silicon photodetectors with decoupled structures: resonant APDs and UTC photodiodes," IEEE J. Sel. Top. Quantum Electron. **20**, 3802214 (2014).
22. H.-Y. Zhao, Naseem, A. H. Jones, R.-L. Chao, Z. Ahmad, J. C. Campbell, and J.-W. Shi, "High-speed avalanche photodiodes with wide dynamic range performance," J. Lightwave Technol. **37**, 5945–5952 (2019).
23. B. Wang, Z. Huang, X. Zeng, R. Wu, W. V. Sorin, D. Liang, and R. G. Beausoleil, "A compact model for Si-Ge avalanche photodiodes," in *IEEE 15th International Conference on Group IV Photonics (GFP)* (2018), pp. 109–110.

24. D. R. Gozzard, L. E. Roberts, J. T. Spollard, P. G. Sibley, and D. A. Shaddock, "Fast beam steering with an optical phased array," Opt. Lett. **45**, 3793–3796 (2020).
25. K. Van Acoleyen, K. Komorowska, W. Bogaerts, and R. Baets, "One-dimensional off-chip beam steering and shaping using optical phased arrays on silicon-on-insulator," J. Lightwave Technol. **29**, 3500–3505 (2011).
26. D. Kwong, A. Hosseini, Y. Zhang, and R. T. Chen, "1 × 12 unequally spaced waveguide array for actively tuned optical phased array on a silicon nanomembrane," Appl. Phys. Lett. **99**, 051104 (2011).
27. D. Dai, M. J. W. Rodwell, J. E. Bowers, Y. Kang, and M. Morse, "Derivation of the small signal response and equivalent circuit model for a separate absorption and multiplication layer avalanche photodetector," IEEE J. Sel. Top. Quantum Electron. **16**, 1328–1336 (2010).
28. J.-M. Lee, S.-H. Cho, and W.-Y. Choi, "An equivalent circuit model for a Ge waveguide photodetector on Si," IEEE Photon. Technol. Lett. **28**, 2435–2438 (2016).
29. B. Wang, Z. Huang, X. Zeng, W. V. Sorin, D. Liang, M. Fiorentino, and R. G. Beausoleil, "A compact model for Si-Ge avalanche photodiodes over a wide range of multiplication gain," J. Lightwave Technol. **37**, 3229–3235 (2019).
30. D. Dai, H.-W. Chen, J. E. Bowers, Y. Kang, M. Morse, and M. J. Paniccia, "Equivalent circuit model of a Ge/Si avalanche photodiode," in *6th IEEE International Conference on Group IV Photonics* (2009), pp. 13–15.
31. M.-J. Lee, H.-S. Kang, and W.-Y. Choi, "Equivalent circuit model for Si avalanche photodetectors fabricated in standard CMOS process," IEEE Electron Device Lett. **29**, 1115–1117 (2008).
32. D. Dai, H.-W. Chen, J. E. Bowers, Y. Kang, M. Morse, and M. J. Paniccia, "Resonant normal-incidence separate-absorption-charge-multiplication Ge/Si avalanche photodiodes," Opt. Express **17**, 16549–16557 (2009).
33. Y. Kang, H.-D. Liu, M. Morse, M. J. Paniccia, M. Zadka, S. Litski, G. Sarid, A. Pauchard, Y.-H. Kuo, H.-W. Chen, W. S. Zaoui, J. E. Bowers, A. Beling, D. C. McIntosh, X. Zheng, and J. C. Campbell, "Monolithic germanium silicon avalanche photodiodes with 340 GHz gain-bandwidth product," Nat. Photonics **3**, 59–63 (2009).
34. B. Shi, F. Qi, P. Cai, X. Chen, Z. He, Y. Duan, G. Hou, T. Su, S. Li, W. Chen, C. Hong, R.-C. Yu, and D. Pan, "106 Gb/s normal-incidence Ge/Si avalanche photodiode with high sensitivity," in *Optical Fiber Communication Conference* (2020), paper M3D.2.
35. C.-L. Hsin and C.-H. Chou, "Buffer-free Ge/Si by rapid melting growth technique for separate absorption and multiplication avalanche photodetectors," IEEE Electron Device Lett. **40**, 945–948 (2019).
36. M. Huang, T. Shi, P. Cai, L. Wang, S. Li, W. Chen, C.-Y. Hong, and D. Pan, "25 Gb/s normal incident Ge/Si avalanche photodiode," in *Systematic Paris Region Systems and ICT Cluster* (2014), pp. 1–3.